The Astronomical Journal, 171:270 (15pp), 2026 May https://doi.org/10.3847/1538-3881/ae4a99

HATPI Preperihelion Time-series Photometry of the Interstellar Comet 3I/ATLAS

Joel D. Hartman[1], Gáspár Á. Bakos[1], Andrés Jordán[2,3,4], Sarah Thiele[1], Zoltán Csubry[1], Geert Jan Talens[5], Attila Bódi[1], Sándor Pigai[6], István Domsa[6], Anthony Keyes[1], Vincent Suc[2,4], Adriana Gaitan[1], and Antoine Thibault[7]
[1] Department of Astrophysical Sciences, Princeton University, NJ 08544, USA
[2] Facultad de Ingeniería y Ciencias, Universidad Adolfo Ibáñez, Av. Diagonal las Torres 2640, Peñalolén, Santiago, Chile
[3] Departamento de Astronomía, Universidad de Chile, Casilla 36-D, Santiago, Chile
[4] Obstech/El Sauce Observatory, Coquimbo, Chile
[5] Denys Wilkinson Building, Department of Physics, University of Oxford, OX1 3RH, UK
[6] Hungarian Astronomical Association, Hungary
[7] Observatoire astronomique de l'Université de Genève, Chemin Pegasi 51, CH-1290 Versoix, Switzerland
Received 2025 December 19; revised 2026 February 12; accepted 2026 February 24; published 2026 April 2

Abstract

The Hungarian-made Automated Telescope PI Steradians (HATPI) is a recently commissioned time-domain facility at Las Campanas Observatory, Chile, that uses 64 wide-angle, 9.6 cm diameter lenses and back-illuminated CCDs, yielding a mosaic field-of-view of 7100 square arcdegrees, observing the night sky at a cadence of 45 s and a spatial scale of $19\farcs7$ pixel^{-1}. In this paper, we present moving object time-series photometry with this facility, focusing on the interstellar comet 3I/ATLAS, which was first robustly recovered by HATPI on the night of 2025 July 2 (one night after its discovery) at a Gaia G-band magnitude of $G = 17.796 \pm 0.082$ mag (± 0.030 mag systematic uncertainty). The comet then increased in brightness to $G = 14.071 \pm 0.073$ mag ± 0.030 mag by 2025 September 13, after which it became unobservable by HATPI as it approached perihelion. Before 3I/ATLAS achieved a brightness of $G = 16.396 \pm 0.029$ mag ± 0.030 mag on 2025 August 6, it could be detected when stacking all HATPI observations from a single night, while after this date it is sufficiently bright to detect in individual 45 s exposures. We do not detect evidence for significant short-time-scale variations in the brightness of 3I/ATLAS after August 6. Compared to other light curves in the literature, the HATPI photometry exhibits a somewhat steeper rise in brightness with decreasing heliocentric distance, r_H. The HATPI magnitudes are well-fit as a power law function of r_H, with an exponential index of $n = 5.167 \pm 0.095$, over the range $2.14\ \mathrm{au} < r_H < 4.44\ \mathrm{au}$, compared to $n = 3.94 \pm 0.10$ when fitting together with other observations in the literature. We find that the phase function is constrained to $\beta = 0.0552 \pm 0.0032\ \mathrm{mag\ deg^{-1}}$.

Unified Astronomy Thesaurus concepts: Comets (280); Time domain astronomy (2109)

Materials only available in the online version of record: machine-readable table

1. Introduction

Comet 3I/ATLAS (initially dubbed C/2025 N1) was discovered by the ATLAS survey on 2025 July 1 (L. Denneau et al. 2025). The object has an extreme hyperbolic orbit, indicating an interstellar origin. It is the third such object discovered to date (the previous two being 1I/'Oumuamua and 2I/Borisov, K. J. Meech et al. 2017; G. Borisov et al. 2019).

Given the rare and fleeting opportunity to study a solid body of interstellar origin, 3I/ATLAS has been the target of significant observational efforts, including imaging (M. R. Combi et al. 2025; M. A. Cordiner et al. 2025; W. B. Hoogendam et al. 2025a; D. Jewitt et al. 2025; C. M. Lisse et al. 2025a; N. X. Roth et al. 2026; T. Scarmato 2025a, 2025b; D. Z. Seligman et al. 2025; M. Serra-Ricart et al. 2026; Z. Xing et al. 2025; Q. Zhang & K. Battams 2026; H. Tan et al. 2026; M.-T. Hui et al. 2026), time-series photometry (J. Beniyama 2025; B. T. Bolin et al. 2025; C. O. Chandler et al. 2025; R. de la Fuente Marcos et al. 2025; T. M. Eubanks et al. 2025; A. D. Feinstein et al. 2025; T. T. Frincke et al. 2025; D. Jewitt & J. Luu 2025; T. Kareta et al. 2025; C. M. Lisse et al. 2025a; J. Martinez-Palomera et al. 2025; L. E. Salazar Manzano et al. 2025; T. Santana-Ros et al. 2025; D. Z. Seligman et al. 2025; J. Tonry et al. 2025; J. M. Trigo-Rodríguez et al. 2025; Q. Ye et al. 2025; Q. Zhang & K. Battams 2026), spectroscopy (A. Alvarez-Candal et al. 2025; M. Belyakov et al. 2025; M. A. Cordiner et al. 2025; I. M. Coulson et al. 2026; R. de la Fuente Marcos et al. 2025; J. T. Hinkle et al. 2025; W. B. Hoogendam et al. 2025a; 2025b; D. Hutsemékers et al. 2026; T. Kareta et al. 2025; C. M. Lisse et al. 2025a; T. H. Puzia et al. 2025; C. Opitom et al. 2025; R. Rahatgaonkar et al. 2025; N. X. Roth et al. 2026; L. E. Salazar Manzano et al. 2025; T. Santana-Ros et al. 2025; D. Z. Seligman et al. 2025; J. M. Trigo-Rodríguez et al. 2025; B. Yang et al. 2025; M. Belyakov et al. 2026; C. M. Lisse et al. 2026; W. B. Hoogendam et al. 2026), time-domain radio observations (B. Jacobson-Bell et al. 2025; S. Z. Sheikh et al. 2025), and polarimetry (S. Choi et al. 2026; Z. Gray et al. 2025).

These observations have in turn inspired a number of theoretical investigations into the physical properties and Galactic origin of the object (R. Cloete et al. 2025; Y. Guo et al. 2025; A. Hibberd et al. 2025; M. J. Hopkins et al. 2025; E. Keto & A. Loeb 2026; 2025b; E. Keto & A. Loeb 2025; F. Neukart 2025; X. Pérez-Couto et al. 2025; G. Ahuja & S. Ganesh 2025, 2026; A. G. Taylor & D. Z. Seligman 2025; J. C. Forbes & H. Butler 2026; R. Maggiolo et al. 2026; T. Scarmato 2025b; T. Scarmato & A. Loeb 2026;

A. Yaginuma et al. 2026) and proposals for missions to encounter the object (A. Hibberd et al. 2026) or to perform novel observations of it (M. Barbieri & A. Loeb 2026).

In this paper, we contribute preperihelion time-series photometry of 3I/ATLAS obtained by the Hungarian-made Automated Telescope PI Steradians (HATPI) facility. HATPI is a high-cadence, moderately high-spatial resolution time-domain survey that uses 64 fast small telescopes in a mosaic configuration to monitor the full sky visible (above the horizon by at least approximately 35 degrees) from Las Campanas Observatory in Chile. Some of the key science aims of the HATPI facility are to discover long-period transiting giant planets, bright rapidly evolving transients, and small asteroids moving quickly past the Earth. The orbit of 3I/ATLAS brought it across the southern sky during 2025 May–September as it approached perihelion. As a result, it was observed by HATPI.

In the following section, we discuss the HATPI instrument, the observations of 3I/ATLAS, and our process for extracting time-series photometry for this moving object. In Section 3, we analyze the light curve in the context of previously reported time-series observations of 3I/ATLAS and use it to measure the heliocentric index of 3I/ATLAS through the HATPI bandpass. We conclude in Section 4.

2. Data Collection and Processing

In this section, we describe the HATPI instrument, the general data processing methods for the instrument that are relevant to the 3I/ATLAS observations, the observations of 3I/ATLAS, and the additional analysis processes applied specifically to the observations of this object to derive a light curve for it.

2.1. The HATPI Instrument

A thorough discussion of the HATPI instrument and data analysis pipeline will be provided in an upcoming paper (Bakos et al. 2026, in preparation), here we provide a brief summary.

The HATPI instrument is located at Las Campanas Observatory in Chile, which is managed by the Carnegie Institution for Science. The instrument uses 64 Mitakon 154 mm $f/1.6$ lenses, each with a diameter of 96 mm, together with 64 MicroLine ML230 cameras from the Finger Lakes Instrumentation company, each with a E2V CCD230-42 2048×2048 back-side-illuminated detector, to observe a combined mosaic field of view of 7055 square degrees (i.e., 17.1% of the full celestial sphere, or 0.7π steradians) at a plate scale of $19\farcs7\,\mathrm{pixel}^{-1}$. This massive field of view is observed at a cadence of 45 s, with all 64 cameras observing synchronously.

Observations are obtained through a custom broadband filter that covers the wavelength range $430\,\mathrm{nm} < \lambda < 890\,\mathrm{nm}$ ($\lambda = 660$ nm central wavelength). While not equivalent, it is fairly close to the Gaia G bandpass which covers ∼330 nm to ∼1050 nm, or ∼400 nm to ∼860 nm at half maximum transmissivity. We use Gaia photometry to calibrate the photometry from HATPI, and report HATPI measurements as G-band measurements, though it should be noted that the HATPI bandpass is not identical to the G bandpass.

At new Moon, and in uncrowded regions of the sky, HATPI reaches a 5σ detection threshold of $G = 16.5$ mag in a single exposure. Sources with $G \lesssim 9$ mag are saturated in the HATPI images.

The 64 lens+camera systems (referred to as instrument holder units, or IHUs) are all attached to a single massive equatorial-drive mount. The mount tracks the sky at the sidereal rate for one hour, before slewing back to its initial hour angle position and tracking again. In addition to the general tracking that is provided by the mount, each IHU has three separate motors that allow for independent microtracking and focus corrections of that IHU. As a result, the pointing is stable at the subpixel level at the centers of each of the 64 individual fields forming the mosaic, and to the pixel level across the entire mosaic, over the course of each 1 hr tracking period.

Note that because HATPI tracks at the sidereal rate, 3I/ATLAS moves slightly with respect to the camera pointing over the course of each 45 s exposure. The maximum motion of 3I/ATLAS within a single exposure over the time window of the observations presented here is $\sim 1\farcs3$, which is less than 0.07 pixels. Because this is less than 0.1 pixels, no special corrections are made for the slight elongation of 3I/ATLAS in the images compared to point sources.

2.2. HATPI Image Processing

The images gathered by HATPI are automatically processed in real-time by server computers located in the HATPI enclosure at Las Campanas. The processing steps relevant to observations of moving objects include CCD image calibration, astrometry, and image subtraction. A MariaDB database is used to keep track of the observations and data analysis products.

Standard CCD calibration steps, including overscan correction, trimming, dark-current and bias correction, masking of bad pixels and columns, and flat-fielding, are carried out using tools in the FITSH package (A. Pál 2012). Master bias, dark, and sky-flat calibration images are obtained nightly (conditions permitting). Sky-flats are used to correct for small-scale variations in the sensitivity, while dome-flats (obtained using a hand-mountable luminescent flat-field screen) are used to correct for large-scale variations in sensitivity.

An astrometric solution is derived for each of the calibrated frames using the Gaia Data Release 2 (DR2) point-source catalog (Gaia Collaboration et al. 2018) as the astrometric reference. We use DR2 rather than the more recent Data Release 3 (DR3) because DR3 was not yet available at the time that the processing pipeline was developed. In order to maintain long-term stability of the data products, we intend to use DR2 for the duration of the HATPI project. Astrometric and photometric differences between DR2 and DR3 are negligible at the precision of HATPI. The Gaia catalog is matched to the sources detected in the HATPI images using a custom-built astrometry package that is based in part on the astrometry.net (D. Lang et al. 2010) software and the FITSH tools. The World Coordinate System (WCS) solution determined for each image is stored in a database to facilitate the quick identification of images covering a particular location on the sky. The median error in the astrometric solution for HATPI observations of 3I/ATLAS is $0\farcs95$.

Optimal image subtraction (C. Alard & R. H. Lupton 1998) is performed for each calibrated frame using the FITRANS and FICONV tools within the FITSH package. The subtraction is performed against an empirical reference image constructed

from ∼100 observations of the same field, with the same IHU, obtained during clear weather conditions, within a few days of new Moon. The calibrated image is spatially registered to the reference image using FITRANS and then FICONV is used to find an optimal transformation to apply to the reference image to match the background, flux scale, and point-spread function (PSF; via convolution) of the registered calibrated image before performing the subtraction. A discrete matrix, with components represented as polynomials in space over the image, is used to parameterize the convolution kernel.

2.3. Observations of 3I/ATLAS

In order to identify HATPI observations of the interstellar comet 3I/ATLAS, we first made use of the JPL Horizons Ephemeris Service (generated with SPICE kernel DE441, with the most recent 3I/ATLAS solution at the time of writing being JPL#36) to determine the apparent R.A./decl. position of 3I/ATLAS, as seen from Las Campanas Observatory, at 30 minutes intervals spanning the time period 1 2025 May through 2025 September 30. In practice, the query was performed multiple times over this period and the full data analysis process described below was carried out as new observations continued to be gathered. Although the orbit of 3I/ATLAS has continued to be refined over time, its position was always known with significantly higher precision than the spatial resolution of HATPI.

Having obtained the ephemerides of 3I/ATLAS, we queried our database of WCS solutions to identify all images covering the position of 3I/ATLAS at the time of observation. Specifically, given position (R.A.$_i$, decl.$_i$) at time t_i, we selected all images obtained at times between $(t_{i-1} + t_i)/2$ and $(t_i + t_{i+1})/2$ containing position (R.A.$_i$, decl.$_i$). We then perform a monotonic cubic spline interpolation (M. Steffen 1990) of the tabulated R.A. and decl. values to determine a more precise estimate of the position at the time of each observation and use the WCS solution for the reference image to evaluate the X and Y pixel position of 3I/ATLAS on the subtracted images.

We find that there is a total of 15,317 individual HATPI images which cover the spatial position of 3I/ATLAS, which were obtained between 2025 May 1 and 2025 September 13. A total of 6238 of these images were collected after 2025 July 2, the date on which 3I/ATLAS first became detectable in the (stacked) HATPI images. Table 1 lists the nights on which HATPI observations of 3I/ATLAS are available. 3I/ATLAS was observed in total by nine different HATPI IHUs, in 33 different distinct fields. The gaps in the observations are due to poor weather conditions at Las Campanas Observatory that prevented the HATPI system from operating. Unfortunately, the weather was unusually poor during July and August, resulting in longer-than-usual gaps in the data.

Figures 1 and 2 show some of the 1 hr stacked difference images of 3I/ATLAS from nights in which the comet was formally detected with 3σ confidence in the nightly binned HATPI light curve (Section 2.4).

2.4. Photometry of 3I/ATLAS

We used the FIPHOT tool from the FITSH package to perform forced aperture photometry of 3I/ATLAS on the subtracted images. For each image, photometry was performed at the R.A./decl. position of the object on that image, determined from the JPL Horizons ephemeris. We performed the photometry using three fixed circular apertures of radii 1.45, 1.95, and 2.35 pixels, corresponding to angular radii of 28.″6, 38.″4, and 46.″3, respectively (photometry interpolated to a fixed 7×10^4 km linear aperture is presented in Section 3). The FIPHOT tool uses the transformation between the reference and calibrated images determined by FICONV (Section 2.2) to correct the photometry for changes in the flux scale and in the shape of the PSF. The resulting light curves are thereby corrected for atmospheric and instrumental variations and can be effectively treated as ensemble-corrected relative flux measurements.

The flux values measured in ADUs are tied to the reference used for the image subtraction. There are a total of 33 references that contributed to the observations of 3I/ATLAS (one for each IHU/field combination in which 3I/ATLAS was observed), each on its own flux scale. To tie the photometry from the different references to a common scale we use Gaia DR2 G and $BP - RP$ catalog photometry measurements. For each reference we find a polynomial transformation from the instrumental reference magnitudes, calculated directly from the reference fluxes, to the Gaia G magnitude. The transformation depends on the X and Y positions of the sources, and their $BP - RP$ colors. We measure an average uncertainty of 0.030 mag on this transformation, based on the standard deviation of the differences between the Gaia catalog G magnitudes and the instrumental magnitudes transformed to the Gaia system for stars used in the fit.

This same transformation can also be cast as a flux scaling factor s, such that $G = -2.5 \log_{10}(sf)$, where f is the flux measured on the reference system, and G is the magnitude on the Gaia G-band system. We apply this scaling factor s to the subtracted image flux measurements of 3I/ATLAS, assuming a value of $BP - RP = 1.0$ mag for the color of the comet (slightly redder than the Solar value of $BP - RP = 0.85$ mag, R. Andrae et al. 2018, based on early photometry of 3I/ATLAS indicating a color that is redder than the Sun). Note that the transformation does not have a sensitive dependence on color. Changing the assumed $BP - RP$ color by 0.15 mag leads to a < 0.02 mag systematic shift in the inferred G magnitude and a 0.003 mag standard deviation in the resulting light curve due to each IHU/field having a slightly different color term. Although the color of 3I/ATLAS has evolved over time, we choose to fix the color in the transformation to Gaia so that the resulting light curve can be more directly interpreted as the light curve measured through the HATPI 430 to 890 nm bandpass.

2.5. Cleaning Contaminated and Problematic Measurements

There are a number of effects that can produce artificial variations in the HATPI light curve of a moving object such as 3I/ATLAS. Here, we describe our methods for identifying affected observations, so that they may be filtered from the data, leaving a clean light curve for analysis.

To flag low quality images (e.g., such as those affected by clouds) that are likely to negatively impact the photometry for many objects, including 3I/ATLAS, we make use of subtracted image statistics that are calculated for all subtracted frames by the HATPI data analysis pipeline and that are recorded in a database. We flag subtracted images with a mean pixel value greater than 20 ADU or less than −15 ADU, or with a standard deviation greater than 400 ADU, or a median absolute deviation (MAD) greater than 100 ADU, or with a 5

Table 1
Summary of HATPI Observations of 3I/ATLAS

Night	JD[a]	R.A.[a] (deg)	Decl.[a] (deg)	r_H,[a,b] (au)	Δ,[a,c] (au)	α,[a,d] (deg)	ν,[a,e] (deg)	N. Obs	N. Clean Obs	N. IHUs
2025 May 1	2460797.8467	288.847363	−18.718188	6.52	6.05	8.12	274.53	299	0	4
2025 May 2	2460798.8453	288.743496	−18.714663	6.49	6.00	8.09	274.60	303	303	4
2025 May 3	2460799.8443	288.635249	−18.711415	6.45	5.95	8.07	274.67	310	126	4
2025 May 4	2460800.8425	288.522631	−18.708477	6.42	5.90	8.04	274.75	227	0	4
2025 May 5	2460801.8630	288.402761	−18.705727	6.39	5.85	8.00	274.82	177	130	4
2025 May 8	2460804.8393	288.025477	−18.699409	6.29	5.70	7.87	275.05	244	244	5
2025 May 9	2460805.8643	287.885565	−18.697792	6.25	5.65	7.82	275.13	164	0	5
2025 May 10	2460806.8156	287.751215	−18.696554	6.22	5.60	7.77	275.21	306	105	6
2025 May 11	2460807.8101	287.605774	−18.695501	6.19	5.55	7.72	275.29	292	157	6
2025 May 19	2460815.6971	286.264719	−18.696346	5.92	5.18	7.12	275.95	43	43	1
2025 May 20	2460816.7838	286.052017	−18.697684	5.88	5.13	7.02	276.04	433	428	7
2025 May 22	2460818.7781	285.643396	−18.700733	5.81	5.03	6.81	276.22	450	109	7
2025 May 23	2460819.7756	285.429831	−18.702563	5.78	4.99	6.70	276.31	528	419	7
2025 May 24	2460820.7744	285.209652	−18.704589	5.75	4.94	6.59	276.40	564	548	7
2025 May 25	2460821.6861	285.003334	−18.706551	5.72	4.90	6.48	276.49	55	0	1
2025 May 27	2460823.8288	284.496069	−18.711798	5.64	4.80	6.21	276.69	601	4	7
2025 May 28	2460824.8279	284.249291	−18.714458	5.61	4.76	6.08	276.79	620	405	7
2025 May 29	2460825.8612	283.986835	−18.717325	5.58	4.71	5.93	276.89	111	111	3
2025 May 30	2460826.8246	283.735712	−18.720088	5.54	4.67	5.79	276.99	575	17	7
2025 Jun 1	2460828.8270	283.192772	−18.726059	5.48	4.58	5.49	277.19	252	0	4
2025 Jun 5	2460832.7332	282.050760	−18.737876	5.34	4.42	4.83	277.60	279	12	5
2025 Jun 6	2460833.6968	281.751674	−18.740703	5.31	4.38	4.66	277.70	253	36	6
2025 Jun 8	2460835.6904	281.110289	−18.746230	5.25	4.29	4.28	277.92	353	44	5
2025 Jun 20	2460847.6254	276.606102	−18.756166	4.84	3.84	1.68	279.36	452	191	5
2025 Jun 21	2460848.6315	276.172358	−18.753879	4.81	3.80	1.46	279.50	300	27	5
2025 Jun 22	2460849.6795	275.711174	−18.750773	4.78	3.76	1.27	279.64	202	29	2
2025 Jun 23	2460850.7029	275.251888	−18.746910	4.74	3.73	1.11	279.77	604	57	6
2025 Jun 24	2460851.5864	274.848765	−18.742849	4.71	3.70	1.03	279.90	10	0	1
2025 Jun 26	2460853.8090	273.803436	−18.729723	4.64	3.62	1.11	280.21	72	0	1
2025 Jul 2	2460859.6355	270.869224	−18.670638	4.44	3.44	2.58	281.08	580	281	8
2025 Jul 3	2460860.6327	270.338913	−18.656322	4.41	3.41	2.90	281.23	569	284	8
2025 Jul 4	2460861.6911	269.767082	−18.639606	4.37	3.38	3.25	281.40	502	381	8
2025 Jul 6	2460863.5915	268.718920	−18.605433	4.31	3.33	3.91	281.71	121	66	2
2025 Jul 11	2460868.5703	265.841931	−18.487985	4.15	3.20	5.74	282.56	446	235	7
2025 Jul 15	2460872.5073	263.443857	−18.362997	4.02	3.10	7.27	283.29	66	0	2
2025 Jul 16	2460873.6755	262.712393	−18.319991	3.98	3.08	7.74	283.51	406	93	6
2025 Jul 17	2460874.5018	262.191372	−18.287818	3.95	3.06	8.07	283.67	222	200	4
2025 Jul 21	2460878.6074	259.543760	−18.106427	3.82	2.98	9.74	284.51	439	162	6
2025 Jul 23	2460880.5747	258.246933	−18.006295	3.75	2.94	10.55	284.93	314	97	6
2025 Jul 24	2460881.5169	257.620487	−17.955244	3.72	2.92	10.94	285.14	144	36	3
2025 Jul 25	2460882.5831	256.907046	−17.895042	3.68	2.90	11.38	285.38	337	181	6
2025 Aug 6	2460894.5949	248.703682	−17.040573	3.29	2.74	16.20	288.41	382	301	5
2025 Aug 7	2460895.5907	248.019423	−16.955835	3.26	2.72	16.58	288.70	348	279	5
2025 Aug 8	2460896.5490	247.361838	−16.872492	3.23	2.71	16.93	288.98	203	201	4
2025 Aug 11	2460899.5178	245.331763	−16.603205	3.14	2.69	17.99	289.87	278	225	5
2025 Aug 12	2460900.5732	244.613452	−16.503637	3.10	2.68	18.36	290.21	116	88	4
2025 Aug 13	2460901.5486	243.952204	−16.410022	3.07	2.67	18.68	290.52	336	305	5
2025 Aug 23	2460911.5309	237.357860	−15.374258	2.76	2.61	21.49	294.14	161	161	3
2025 Aug 25	2460913.5081	236.099581	−15.155868	2.70	2.60	21.91	294.95	91	30	2
2025 Sep 8	2460927.4864	227.751630	−13.542803	2.28	2.55	23.17	301.93	41	40	2
2025 Sep 9	2460928.4823	227.194063	−13.425098	2.25	2.55	23.13	302.53	44	44	2
2025 Sep 10	2460929.4807	226.639942	−13.306873	2.22	2.55	23.07	303.14	40	39	2
2025 Sep 11	2460930.4820	226.088892	−13.188132	2.19	2.55	22.99	303.77	12	4	2
2025 Sep 13	2460932.4796	225.003510	−12.950752	2.14	2.54	22.77	305.08	17	16	1
2025 Sep 14	2460933.4797	224.466869	−12.831684	2.11	2.54	22.63	305.76	23	0	1

Notes.
[a] Median value among observations from that night.
[b] Heliocentric distance of 3I/ATLAS.
[c] Geocentric distance of 3I/ATLAS.
[d] Sun–3I/ATLAS–Earth angle.
[e] Apparent true anomaly angle of the target's heliocentric orbit position.

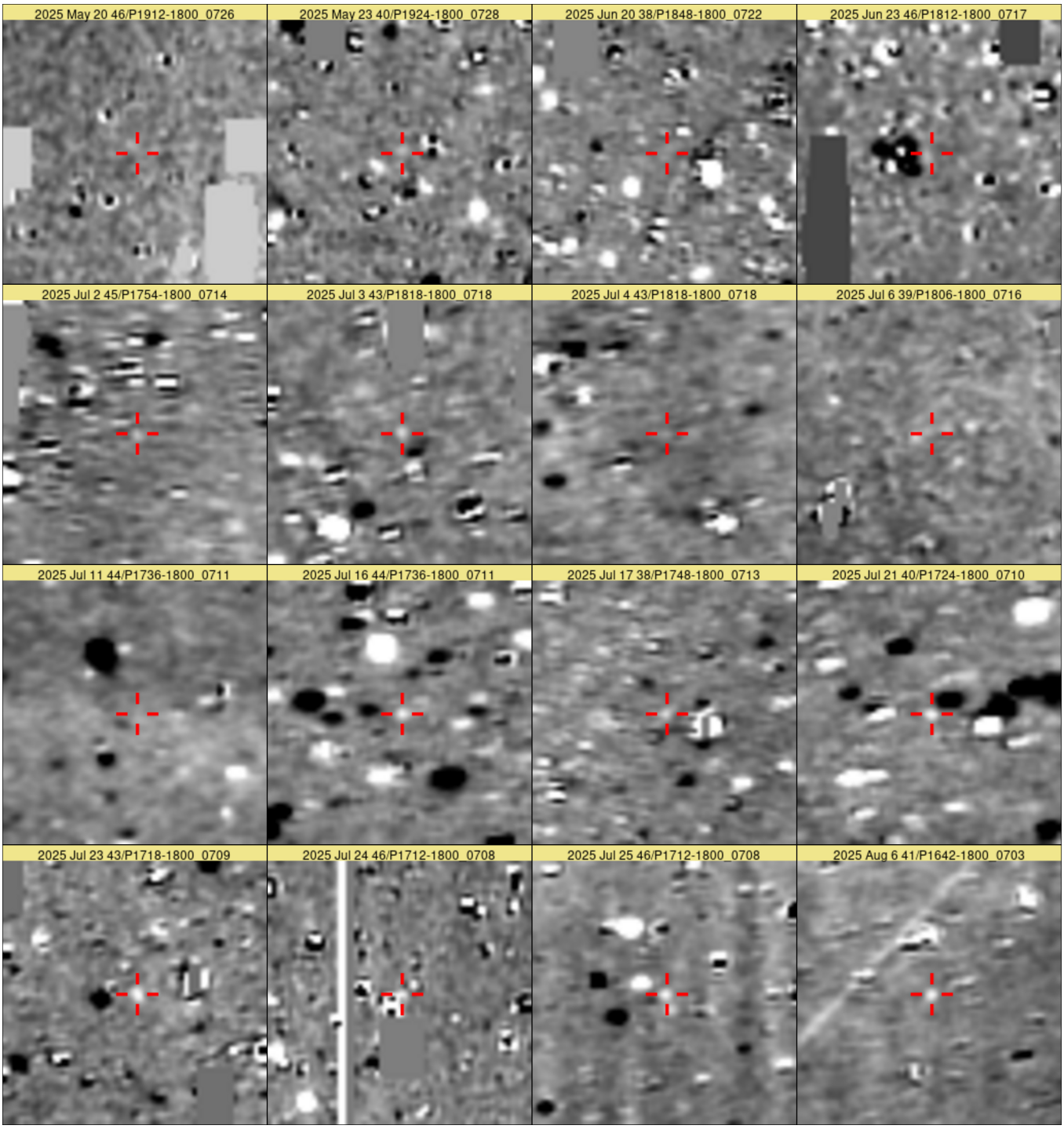

Figure 1. One hour stacked HATPI subtracted images of 3I/ATLAS from each of the nights on which 3I/ATLAS is formally detected with 3σ confidence in the full-night binned light curve (nights corresponding to blue points in Figure 4(c)). Individual 45 s exposures that are flagged as problematic (Section 2.5) are excluded from the stacking. Each image stamp is $21' \times 21'$, displayed with north up and east to the left. The red lines indicate the position of the nucleus of 3I/ATLAS in the center of each stamp. Gray rectangular regions are masked from the image subtraction process due to the presence of saturated stars. Other sources are variable objects, residual Poisson noise from bright stars, or other systematic residuals from poor subtractions (typically most notable for bright stars). Because 3I/ATLAS was at low Galactic latitude, the density of such objects is high in these stacked subtracted images. Individual 45 s exposures are aligned on the position of 3I/ATLAS before stacking, causing background variable star sources (which can be either positive or negative) to show trails. For each night, we show a single IHU/field as indicated in the labels after the date, while additional IHU/fields may be available and included in the full-night binned light curves. Note that the stacked images are for display purposes only. The photometry is performed on the individual 45 s exposures, and binning is then performed on the photometric measurements rather than the images. The detections on May 20, May 23, June 20, June 23, July 6, July 11, and July 21 are likely affected by contamination from neighboring variable sources and are excluded from the analysis. The first night on which we consider the recovery of 3I/ATLAS to be reliable is 2025 July 2. Additional stamps are shown in Figure 2.

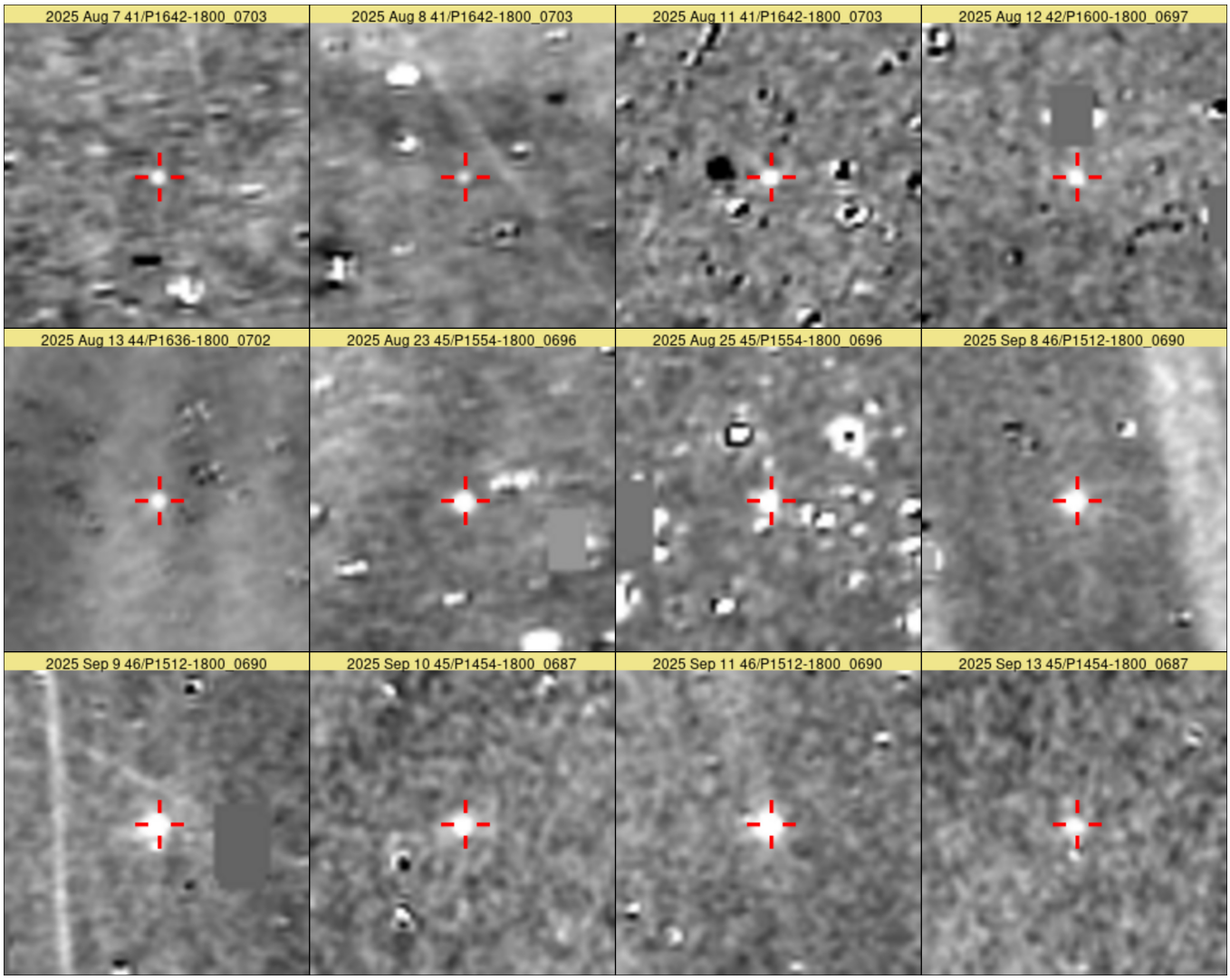

Figure 2. A continuation of Figure 1. Here, we show observations from August 7 through September 13.

percentile value less than −400 ADU, or a 95 percentile value greater than 400 ADU as problematic. In addition to these cuts, we also impose a constraint on the mean of tiled medians statistic. This statistic is computed by splitting the subtracted frame into a grid of tiles, calculating the median of each tile, and then taking the mean of these different median values. We flag images where the statistic is greater than 20 ADU or less than −20 ADU. All of these cuts are chosen based on a visual inspection of the time-series values of the statistic over the observations containing 3I/ATLAS, with thresholds imposed where there is a clear deviation in the distribution of values between a long tail of outliers and a clustering of points around a typical range. A total of 143 out of the 15,317 observations of 3I/ATLAS are flagged.

The majority of HATPI images contain satellite trails. Although only a small fraction of pixels is affected by satellite trails in a given image, in a collection of more than 10,000 images it is likely that a given target is impacted by satellite trails at least several times (e.g., A. S. Borlaff et al. 2025). We make use of a convolutional neural network method to identify pixels in the subtracted frames that are affected by satellite trails. The method will be described in an upcoming paper (Thiele et al. 2026, in preparation). We use these identifications to flag any observations in the HATPI light curve where the photometric aperture contains one or more pixels contaminated by satellites. Altogether, we find that 10 out of the 15,317 observations of 3I/ATLAS are affected.

Due to the motion of 3I/ATLAS across the sky, coupled with the relatively low spatial resolution of the HATPI images, 3I/ATLAS is blended with background stars in a significant fraction of the HATPI observations. The image subtraction method corrects for this blending by subtracting the light of the star, as observed on the reference image. For nonvariable stars, this method works reasonably well; however, enhanced Poisson noise remains in the residual at the location of the star. For bright stars, this can overwhelm the signal from 3I/ATLAS. Additionally, for stars that vary in brightness, a positive or negative variable source may be present in the subtracted image. Blending with variable stars can thus produce artificial variations in the light curve of 3I/ATLAS.

We include in the HATPI light curve a flag indicating observations where a source in the Gaia DR2 catalog with $G < 13$ mag is within $1'$ of 3I/ATLAS. A total of 7412 observations are flagged as such.

To identify those sources that are variable, we made use of any HATPI light curves that are available for them. We also

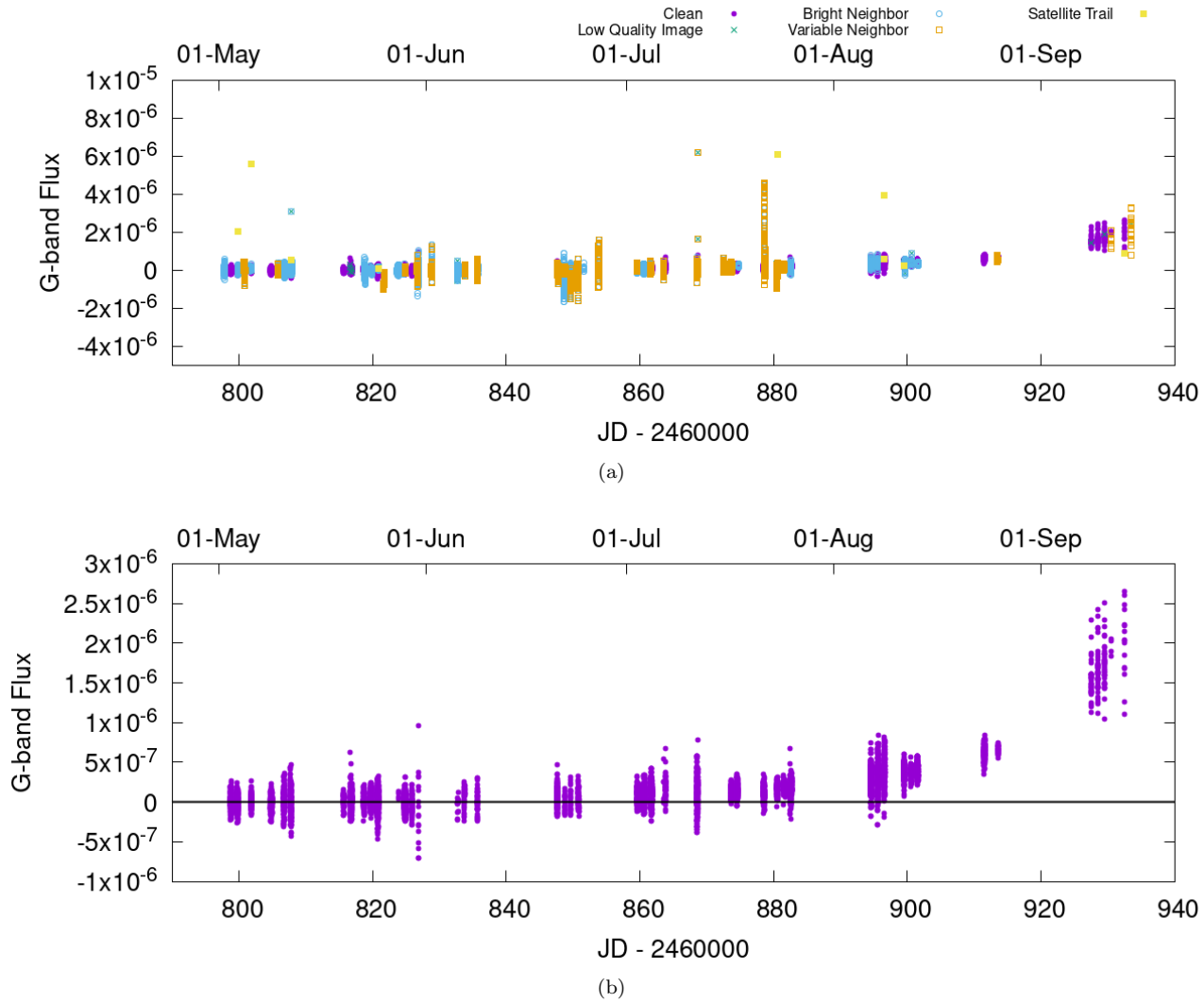

Figure 3. Full, unbinned, HATPI light curves of 3I/ATLAS shown as fluxes F. These are calibrated to the Gaia G-band system such that the Gaia magnitude is equal to $-2.5\log_{10}(F)$. Top: All points are shown, including those that are rejected by the cleaning methods described in Section 2.5. The color coding shows points with different quality flags. Bottom: Same as above but now including only the "clean" points from the top panel.

made use of the ASAS-SN Catalog of Variable Stars (T. Jayasinghe et al. 2019).[8] The HATPI light curves are generally from 2024, though some stars also have 2022 and 2023 light curves available as well. We calculated the Generalized Lomb–Scargle periodogram (M. Zechmeister & M. Kürster 2009) using the implementation in VARTOOLS (J. D. Hartman & G. Á. Bakos 2016), marking any source with a formal log_{10} false alarm probability less than -50 as a potential variable star. A total of 233 of the 1265 stars with HATPI light curves that were within $1'$ of 3I/ATLAS are flagged as potentially variable. We also found 29 stars that are listed as variable in the ASAS-SN catalog and were within $1'$ of 3I/ATLAS in the HATPI observations. Three of the ASAS-SN variables lacked HATPI light curves, and two have HATPI light curves but were not flagged as variable. The remaining 24 ASAS-SN variables were also identified as variables based on their HATPI light curves. An additional flag is added to the HATPI light curve of 3I/ATLAS to note observations where the object was blended with a star identified as potentially variable in this manner. A total of 3,418 observations (out of 15,317 total observations) are flagged as being blended with an identified variable source.

Altogether, combining the flags for problematic images, satellites, contamination from bright neighbors, and contamination from variable stars, we find that 8023 of the observations are flagged as being impacted by one or more of these effects, leaving 7,294 remaining clean observations.

2.6. Photometric Uncertainties

The photometric uncertainties returned by FIPHOT already account for shot noise from the source and the sky background. However, because of the motion of 3I/ATLAS across the sky, changes in the contamination from neighboring sources contribute additional scatter to the photometric measurements. We account for this by imposing a floor on the individual photometric uncertainties. For each measurement, we take the uncertainty to be the maximum of the formal uncertainty from FIPHOT, 1.483 times the MAD of all photometric measurements obtained before 2025 June 28, or 1.483 times the MAD of all measurements obtained on the same night, and with the

[8] Obtained from the ASAS-SN Sky Patrol website https://asas-sn.osu.edu/variables on 2026 February 1.

Table 2
Full Unbinned HATPI Light Curve of 3I/ATLAS

JD (d)	IHU	Field	R.A. (deg)	Decl. (deg)	$Flux_0$[a] (counts)	$eFlux_0$ (counts)
2460797.77285	39	P1906-1800_0725	288.8550012	−18.7184374	$-1.094e-07$	$1.2e-07$
2460797.77334	39	P1906-1800_0725	288.8549511	−18.7184355	$2.060e-08$	$1.2e-07$
2460797.77382	39	P1906-1800_0725	288.8549014	−18.7184337	$-5.273e-08$	$1.2e-07$
2460797.77431	39	P1906-1800_0725	288.8548522	−18.7184318	$3.215e-08$	$1.2e-07$
2460797.77480	39	P1906-1800_0725	288.8548020	−18.7184299	$-1.306e-07$	$1.2e-07$
2460797.77529	39	P1906-1800_0725	288.8547520	−18.7184280	$-4.254e-07$	$1.2e-07$
2460797.77577	39	P1906-1800_0725	288.8547025	−18.7184260	$-1.353e-07$	$1.2e-07$
2460797.77626	39	P1906-1800_0725	288.8546530	−18.7184240	$-1.458e-07$	$1.2e-07$
2460797.77675	39	P1906-1800_0725	288.8546033	−18.7184220	$-1.622e-07$	$1.2e-07$
2460797.77724	39	P1906-1800_0725	288.8545534	−18.7184200	$-1.068e-07$	$1.2e-07$

$Flux_1$[b] (counts)	$eFlux_1$ (counts)	$Flux_2$[c] (counts)	$eFlux_2$ (counts)	Bad Stats[d]	Satellite[e]	BrightNbr[f]	VarNbr[g]
$-6.508e-10$	$1.3e-07$	$5.408e-08$	$1.5e-07$	0	0	1	0
$4.233e-08$	$1.3e-07$	$8.416e-08$	$1.5e-07$	0	0	1	0
$-2.495e-08$	$1.3e-07$	$-2.375e-08$	$1.5e-07$	0	0	1	0
$7.549e-08$	$1.3e-07$	$6.092e-08$	$1.5e-07$	0	0	1	0
$-1.280e-07$	$1.3e-07$	$-1.649e-07$	$1.5e-07$	0	0	1	0
$-3.856e-07$	$1.3e-07$	$-3.915e-07$	$1.5e-07$	0	0	1	0
$-1.034e-07$	$1.3e-07$	$-1.122e-07$	$1.5e-07$	0	0	1	0
$-2.719e-08$	$1.3e-07$	$4.196e-08$	$1.5e-07$	0	0	1	0
$-1.469e-07$	$1.3e-07$	$-1.556e-07$	$1.5e-07$	0	0	1	0
$-9.740e-08$	$1.3e-07$	$-1.254e-07$	$1.5e-07$	0	0	1	0

Notes. This table is published in its entirety in machine-readable format. A portion is shown here for guidance regarding its form and content.
[a] Flux through 28.″6 aperture scaled so that Gaia-band magnitude $G = -2.5\log_{10}(F)$.
[b] Flux through 38.″4 aperture scaled so that Gaia-band magnitude $G = -2.5\log_{10}(F)$.
[c] Flux through 46.″3 aperture scaled so that Gaia-band magnitude $G = -2.5\log_{10}(F)$.
[d] 1 - bad image statistics; 0 - observation okay.
[e] 1 - satellite trail; 0 - no trail.
[f] 1 - contaminated by bright neighbor; 0 - not contaminated.
[g] 1 - contaminated by variable neighbor; 0 - not contaminated.

(This table is available in its entirety in machine-readable form in the online article.)

same IHU/field as the target observation. This process is performed separately for each of the three different photometric apertures used.

2.7. Light Curve of 3I/ATLAS

Figure 3 shows the full unbinned flux light curve of 3I/ATLAS before and after cleaning. The data are available in Table 2.

Figure 4 shows the cleaned light curve binned in time using a weighted mean. We show the result when binning all observations for a given IHU/field on a given night (i.e., an effective 1 hr binning) and when binning together all observations on a given night. For the light curve shown in magnitudes, we indicate the 3σ upper-limit on the brightness when the measured differential flux is within 3σ of zero. We also plot in this figure the expected T magnitude of 3I/ATLAS from JPL/Horizons. This is computed using an expression equivalent to Equation (1) in Section 3, with $M_F = M_V$, $m = 2$, and $\Phi_\alpha \equiv 1.0$. JPL/Horizons adopts $M_V = 12.5$ and $n = 4.5$ for 3I/ATLAS. As seen in Figure 4, these parameters do not provide a tight fit to the HATPI observations. In Section 3, we fit Equation (1) to the HATPI and literature light curves of 3I/ATLAS to obtain best-fit parameters.

The full-night binned light curve shows two potential early detections of 3I/ATLAS on the nights of 2025 May 20 and 2025 May 23, i.e., prior to the discovery, where we measure $G = 19.46 \pm 0.33$ mag, and $G = 18.61 \pm 0.14$ mag, respectively. However, we caution that 3I/ATLAS was in a crowded region of the sky at this time (Galactic latitude $b \approx -11^\circ$) and blending with other variable sources may have contaminated the measurements on these nights. It is worth noting that we also measure a negative flux on the night of 2025 May 29 that is 3σ less than 0. This indicates that some variability contaminated measurements remain, despite our efforts to flag and remove affected observations (Section 2.5). Based on the model fit to the combined HATPI and published light curves of 3I/ATLAS (Section 3), we find that the expected magnitude of 3I/ATLAS on 2025 May 20 is $G = 19.55$ mag, while on 2025 May 23 it is $G = 19.40$ mag. The potential detection on 2025 May 20 is thus within 1σ of its expected value, while the possible 2025 May 23 observation would be 5.6σ brighter than its expected value. Given the overall uncertainty associated with these early measurements, we exclude them from further analysis.

As a further check on potential variability blending, Figure 5 compares the nightly binned light curve, in magnitudes, from the three different apertures used for photometry. On some of the earlier nights in the light curve there are large $>1\sigma$ differences in the binned magnitudes between the different apertures. This is a signal of possible contamination from nearby sources. Nights of particular concern include June 20,

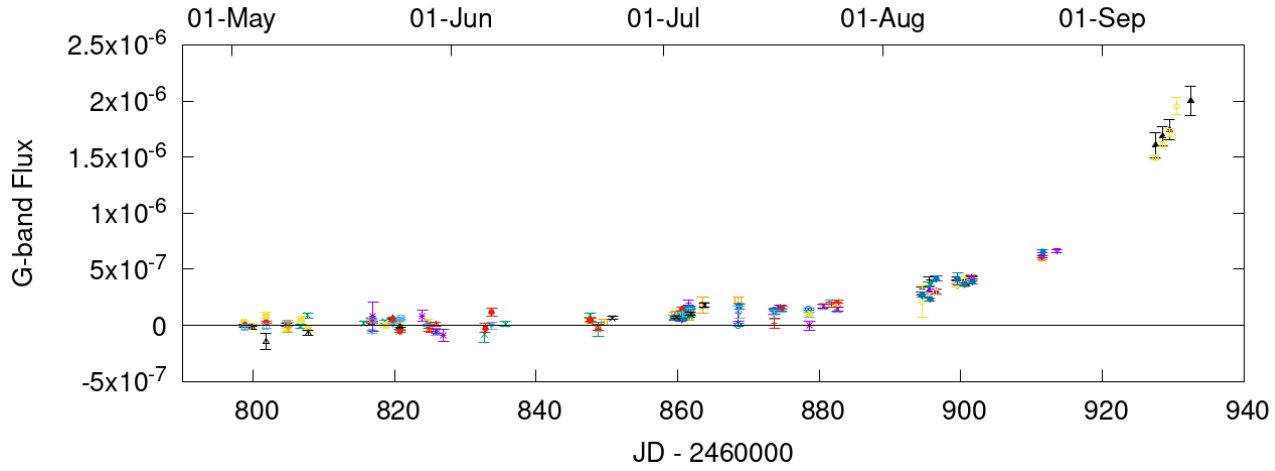

(a)

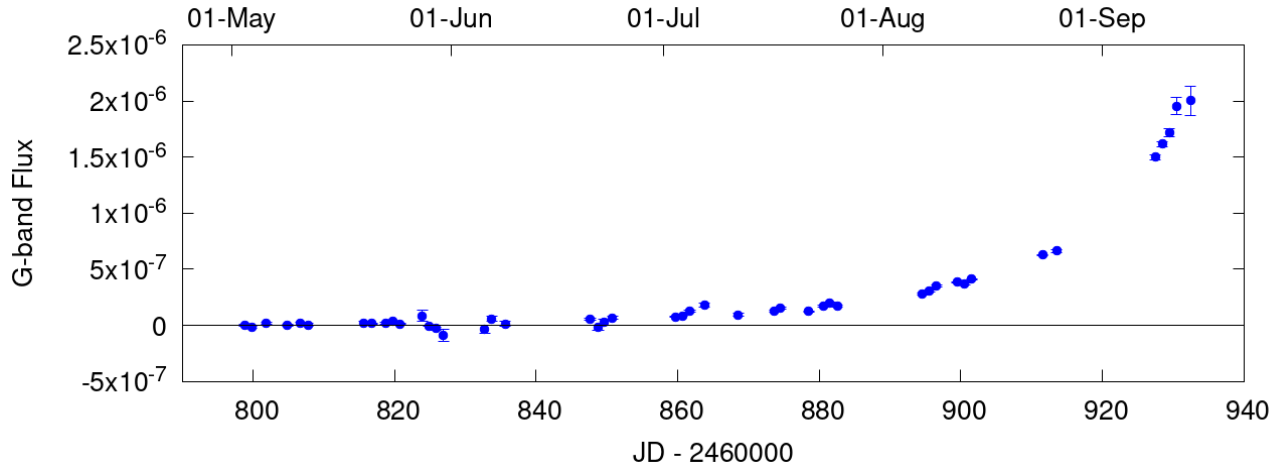

(b)

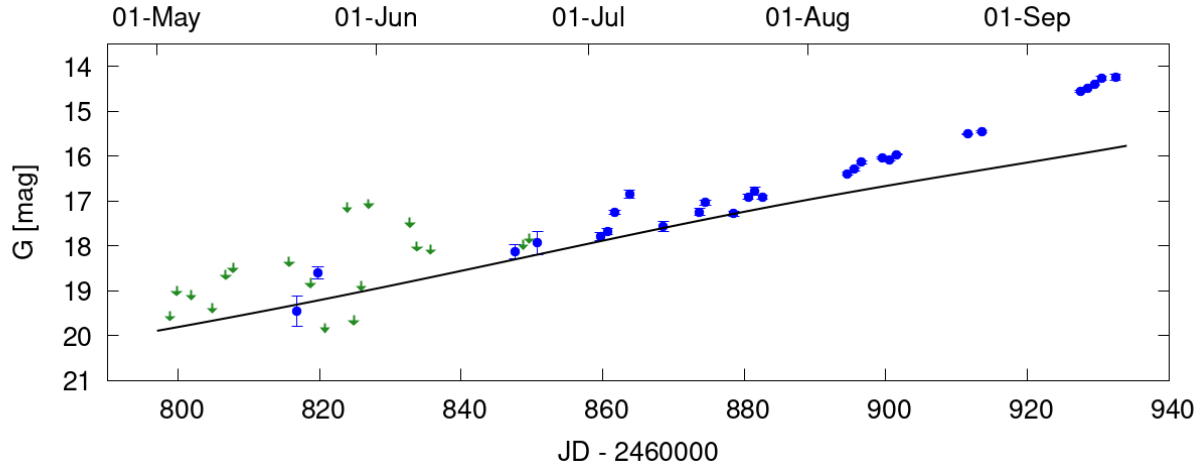

(c)

Figure 4. Top: Clean HATPI light curve of 3I/ATLAS shown as fluxes F on the Gaia G-band system such that the Gaia magnitude is equal to $-2.5\log_{10}(F)$. We bin all observations obtained on a given night by a given IHU/field using the weighted mean. Each point thus represents up to one hour of observations. Different colors indicate the different IHU/fields. Middle: Same as above but now binning together all observations obtained on a given night. Each point in this case represents up to ∼6 hr of observations. Bottom: Same as middle but showing the nightly binned light curve converted to magnitudes. Circles show points for which a nonzero flux is measured with at least 3σ confidence, while arrows indicate 3σ upper limits on the brightness. The solid line shows the expected T magnitude from JPL/Horizons.

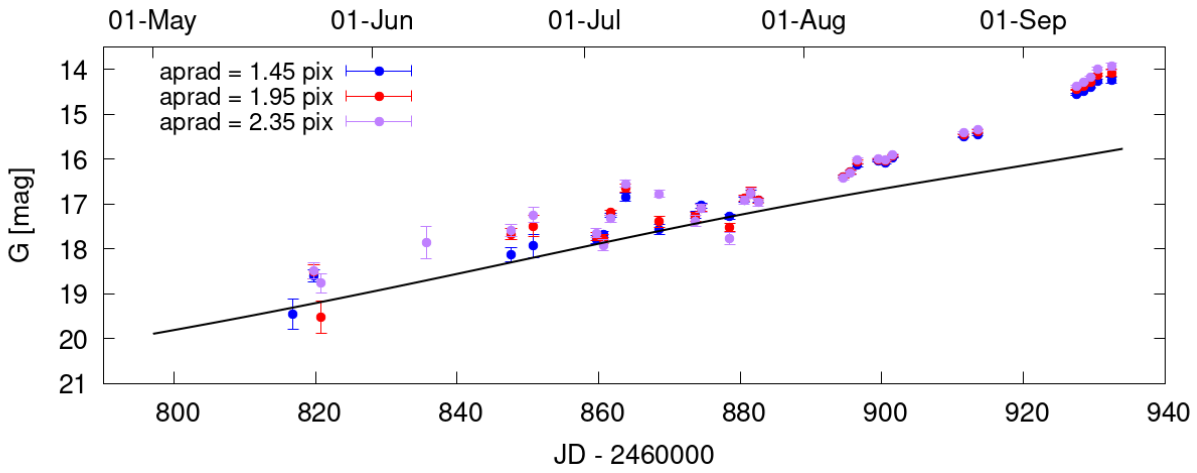

Figure 5. The nightly binned HATPI light curve of 3I/ATLAS for three different concentric, circular apertures. Here, we omit upper-limit measurements. As a result, on some nights fewer than three apertures are displayed. All other figures show the 1.45 pixel aperture measurements. Large inconsistencies between the different apertures for some of the early-time observations indicate measurements that may be contaminated by blending with residual variable sources. At late times, as the cometary tail becomes resolved by HATPI, the largest aperture measurements are systematically brighter than the smaller aperture measurements.

June 23, July 6, July 11, and July 21. We exclude these observations from further analysis, together with the two early observations in May where the flux was formally detected with greater than 3σ confidence.

The first night on which 3I/ATLAS appears to be robustly detected, without additional caution regarding potential contamination, is the night of July 2. On this night we detected a positive flux for 3I/ATLAS with 13σ confidence, and measure $G = 17.796 \pm 0.082$ mag.

Figure 5 also shows systematically brighter measurements for larger apertures during later nights in the light curve (i.e., following 2025 September 8). We attribute this to the cometary tail of 3I/ATLAS extending past the largest aperture on these dates.

To check for variability on shorter timescales, Figure 6 shows the individual, unbinned, photometric light curves from 12 different nights. The first night that we show is 2025 August 6, which is the first night on which 3I/ATLAS is detected with 3σ confidence in individual 45 s HATPI exposures. We do not see any clear evidence of variability at the ~0.2 mag level within any individual night. By August 6 the coma of 3I/ATLAS dominates the light from the system, suppressing any rotational signal from the nucleus. A ~0.3 mag peak-to-peak amplitude, $P = 16.16 \pm 0.01$ hr periodic variation has been reported based on observations obtained in 2025 July (T. Santana-Ros et al. 2025). At this earlier time, the nucleus was still detectable.

3. Discussion

The preperihelion light curve of 3I/ATLAS can be used to measure the heliocentric index n of the comet (the dust production as a function of heliocentric distance, assuming a dependence of $\sim r_H^{-n}$), which in turn depends on the composition of the sublimating material. D. Jewitt & J. Luu (2025) combined photometry of 3I/ATLAS from the Nordic Optical Telescope, together with previously published light curves from the Zwicky Transient Facility (ZTF; Q. Ye et al. 2025), ATLAS (J. Tonry et al. 2025), and TESS (J. Martinez-Palomera et al. 2025) to measure an index of $n = 3.8 \pm 0.3$ over a distance range of 4.6 to 1.8 au. This index is consistent with CO_2 being the dominant sublimating material, as independently indicated by initial spectroscopic observations of the tail (M. A. Cordiner et al. 2025; C. M. Lisse et al. 2025b).

Table 3
Parameters from Fitting Equation (1) to the HATPI and Literature Light Curves

Parameter	Value	Extra Error[a]
n	3.94 ± 0.10	
β (mag deg^{-1})	0.0552 ± 0.0032	
$M_{HATPI,G}$ (mag)	8.03 ± 0.19	0.33
$M_{NOT,R}$ (mag)	8.21 ± 0.16	0.14
$M_{ZTF,g}$ (mag)	9.56 ± 0.18	0.060
$M_{ZTF,r}$ (mag)	8.90 ± 0.19	0.16
$M_{ATLAS,c}$ (mag)	9.63 ± 0.17	0.24
$M_{ATLAS,o}$ (mag)	9.15 ± 0.17	0.13
$M_{ATLAS,w}$ (mag)	9.37 ± 0.18	0.17
$M_{TESS,T}$ (mag)	8.74 ± 0.23	0.30
$M_{SNIFS,g}$ (mag)	9.57 ± 0.17	0.077
$M_{SNIFS,c}$ (mag)	9.25 ± 0.17	0.068
$M_{SNIFS,r}$ (mag)	8.86 ± 0.17	0.062
$M_{SNIFS,o}$ (mag)	8.72 ± 0.17	0.063
$M_{SNIFS,i}$ (mag)	8.58 ± 0.17	0.059
$M_{SNIFS,z}$ (mag)	8.51 ± 0.17	0.066

Note.
[a] Extra error terms added in quadrature to the uncertainties for each light curve so that the best-fit model has χ^2 per degree of freedom equal to 1 for each light curve.

We repeat this analysis, incorporating the HATPI observations, as well as spectrophotometric time-series observations made with the SuperNova Integral Field Spectrograph (SNIFS) on the University of Hawai'i 2.2 m telescope (W. B. Hoogendam et al. 2025b). Following Equation 1 from D. Jewitt & J. Luu (2025), the apparent magnitude of the comet in filter F at a heliocentric distance r_H and geocentric distance Δ is given by

$$m_F = M_F + 2.5\log_{10}(r_H^n \Delta^m) - 2.5\log_{10}(\Phi_\alpha). \quad (1)$$

Here, Φ is the phase function of the comet, which depends on the Sun–object–Earth angle α. M_F is the absolute magnitude of the comet through filter F, which corresponds to the apparent

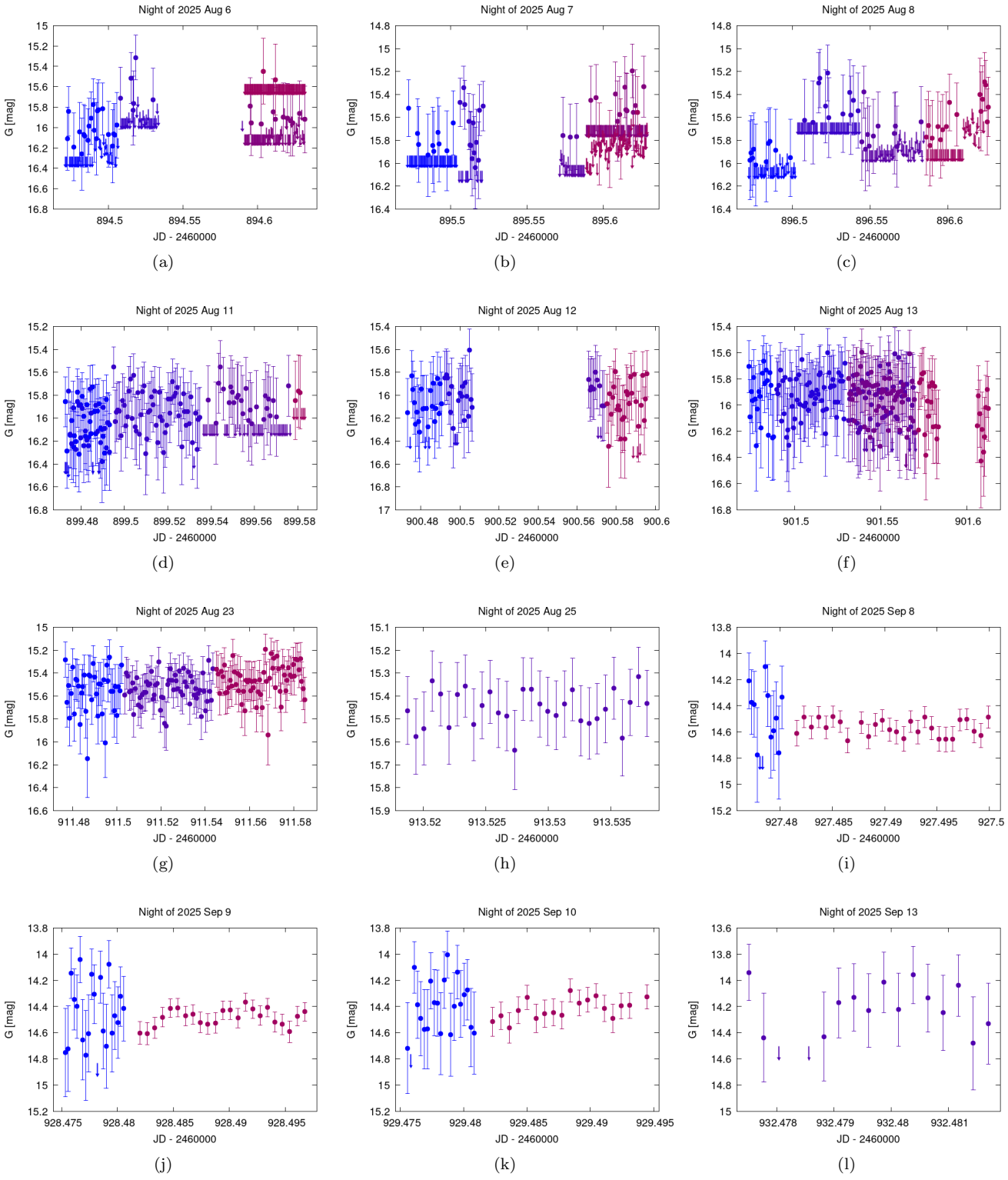

Figure 6. Unbinned 45 s cadence clean light curves of 3I/ATLAS from HATPI for 12 different nights, starting from 2025 August 6, the first night on which 3I/ATLAS is detectable with 3σ confidence in individual HATPI exposures. Different colors indicate different IHU/fields used to observe the target. Arrows show 3σ upper limits on the magnitude. No variability at the $\sim$0.2 mag level is detected within any individual night. We do not show 2025 September 11, on which only four observations were gathered.

magnitude that would be observed from a geocentric distance of 1 au when the comet is at a heliocentric distance of 1 au, and with $\Phi = 1$. The heliocentric and geocentric indices of the comet are n and m, respectively.

As noted by D. Jewitt & J. Luu (2025), one can fix $m \equiv 2$ when using a fixed linear aperture to measure photometry (i.e., an aperture of angular size that varies with the distance to the comet Δ as Δ^{-1}, so that it subtends a fixed linear span at

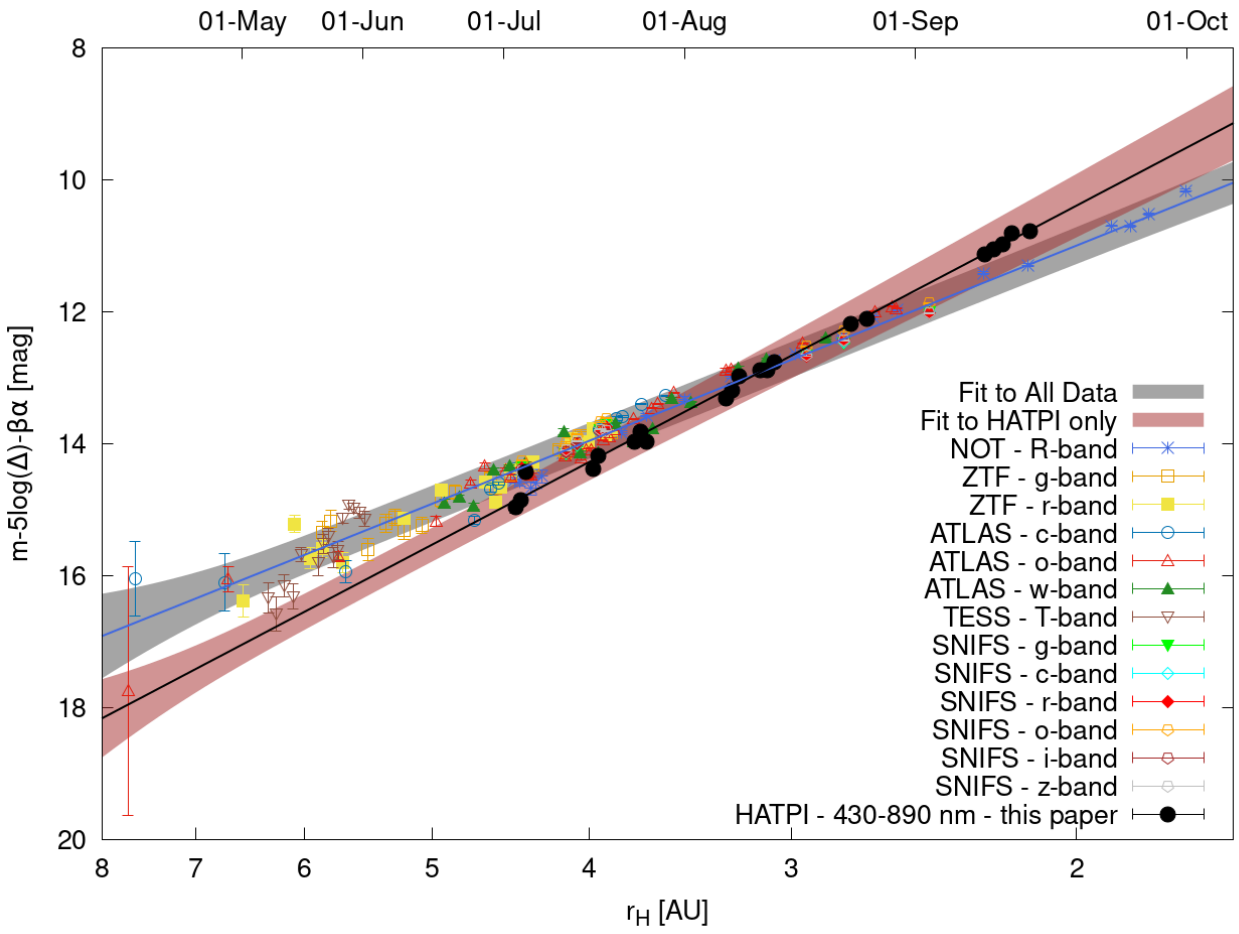

Figure 7. A comparison of the nightly binned clean 7×10^4 km linear-aperture HATPI light curve of 3I/ATLAS to light curves reported in the literature. The ATLAS photometry is taken from J. Tonry et al. (2025), the ZTF photometry from Q. Ye et al. (2025), the TESS photometry from J. Martinez-Palomera et al. (2025), and the NOT photometry from D. Jewitt & J. Luu (2025). We plot the observed magnitude, corrected for the geocentric distance, Δ, and the phase-function $\beta\alpha$, with β fixed to its optimized value of 0.0552 ± 0.0032 mag deg^{-1} for the plot. We plot this as a function of the heliocentric distance r_H, shown on a logarithmic scale. All light curves have been shifted by $M_G - M_F$ to match the optimized HATPI heliocentric magnitude. We show the best-fit power-law model (Equation (1)) when jointly fitting all of the observations, together with the model from fitting only the HATPI observations, while using a prior to constrain β to its jointly optimized value. The bands about each best-fit line show the 1σ confidence interval for the model. The HATPI observations show a steeper increase in brightness with decreasing r_H, with a power-law index of $n = 5.167 \pm 0.095$ compared to $n = 3.94 \pm 0.10$ when fitting all of the data.

the distance of the comet) but when using an aperture of fixed angular size m will in general take a different value. These authors adopted a fixed linear aperture of 10^4 km. Due to the lower spatial resolution of HATPI, we adopt a larger linear aperture of 7×10^4 km, such that the minimum angular aperture of $28\farcs6$ is used at the first clean HATPI observation, when Δ is maximum among the HATPI observations. To estimate the photometry within the fixed linear aperture at each observation, we perform linear interpolation, in calibrated fluxes, between the three different apertures used. The resulting binned data are given in Table 4.

Figure 7 compares the fixed linear aperture HATPI photometry to photometry from the literature, using the same datasets as D. Jewitt & J. Luu (2025), as well as the SNIFS data from W. B. Hoogendam et al. (2025b). In this figure, we also show the result of fitting Equation (1) to the observations. In performing this fit we follow D. Jewitt & J. Luu (2025) in assuming $-2.5 \log_{10}(\Phi(\alpha)) = \beta\alpha$. We jointly fit all observations together, optimizing M_F for each dataset, together with n and β. We performed the fit iteratively, adding a separate error term in quadrature to the uncertainties from each light curve until we achieved χ^2 per degree of freedom equal to unity for each light curve. The best-fit parameters, together with the extra error terms added to each light curve, are listed in Table 3. We find $n = 3.94 \pm 0.10$ and $\beta = 0.0552 \pm 0.0032$ mag deg^{-1}. The final fit has $\chi^2 = 206.9$. There are 218 observations and 16 parameters that are varied, so that the combined reduced χ^2 is 1.02.

The HATPI data show a steeper increase in brightness with decreasing r_H when compared to the literature observations. The difference is mostly seen between the HATPI and Nordic Optical Telescope (NOT) measurements, which extend to the closest heliocentric separations. When we fit the HATPI data alone, applying a prior on β of $\beta = 0.0552 \pm 0.0032$ mag deg^{-1} based on the fit to all of the observations, we find $M_G = 6.50 \pm 0.12$ mag and $n = 5.167 \pm 0.095$. In this case, an extra error of 0.095 mag is added in quadrature to the HATPI light curve uncertainties to achieve a reduced χ^2 of unity.

A difference in the heliocentric index for HATPI is not unexpected given the larger linear aperture used for the HATPI photometry (7×10^4 km for HATPI, compared with 10^4 km for NOT), together with the different bandpass of HATPI (430 nm to 890 nm for HATPI, compared with 568 to 718 nm for the NOT R band).

Table 4
Nightly Binned and Cleaned HATPI Light Curve of 3I/ATLAS shown in Figure 7

JD (d)	$Gmag_0$[a] (mag)	$eGmag_0$[a] (mag)	$Gmag_1$[b] (mag)	$eGmag_1$[b] (mag)	$Gmag_2$[c] (mag)	$eGmag_2$[c] (mag)	Ap. Size[d] (arcsec)	Gmag 7×10^4 km (mag)	eGmag 7×10^4 km (mag)	r_h[e] (au)	Δ[f] (au)	α[g] (deg)	ν[h] (deg)	Nobs[i]	Δt[j] (h)
2460859.69823	17.797	0.082	17.716	0.091	17.66	0.10	28.6	17.796	0.082	4.441	3.440	2.5954	281.0854	281	6.36
2460860.64642	17.682	0.075	17.791	0.098	17.92	0.13	28.8	17.684	0.074	4.410	3.412	2.9015	281.2339	284	5.39
2460861.70327	17.253	0.049	17.198	0.054	17.334	0.069	29.1	17.251	0.046	4.375	3.382	3.2539	281.4020	381	6.34
2460873.66564	17.248	0.086	17.28	0.10	17.38	0.13	32.0	17.260	0.067	3.978	3.078	7.7323	283.5111	93	1.40
2460874.50012	17.040	0.054	17.086	0.069	17.100	0.081	32.2	17.057	0.042	3.950	3.060	8.0670	283.6739	200	5.59
2460880.56973	16.911	0.064	16.873	0.072	16.920	0.088	33.5	16.892	0.048	3.751	2.939	10.5501	284.9306	97	3.28
2460881.47923	16.782	0.092	16.73	0.11	16.76	0.12	33.7	16.755	0.073	3.721	2.923	10.9254	285.1304	36	5.49
2460882.58583	16.924	0.048	16.922	0.061	16.972	0.073	33.9	16.923	0.039	3.685	2.903	11.3830	285.3781	181	5.29
2460894.60229	16.396	0.032	16.396	0.038	16.422	0.043	36.0	16.396	0.029	3.294	2.735	16.2039	288.4154	301	3.84
2460895.59798	16.289	0.033	16.287	0.039	16.320	0.045	36.1	16.287	0.031	3.262	2.724	16.5787	288.6995	279	3.76
2460896.54977	16.137	0.034	16.064	0.036	16.023	0.042	36.3	16.080	0.029	3.232	2.715	16.9312	288.9764	201	3.70
2460899.50209	16.044	0.019	16.015	0.022	16.006	0.026	36.6	16.020	0.018	3.137	2.687	17.9877	289.8696	225	2.65
2460900.50528	16.076	0.029	16.032	0.034	16.009	0.041	36.8	16.039	0.029	3.105	2.678	18.3323	290.1854	88	2.94
2460901.54540	15.964	0.015	15.930	0.017	15.899	0.020	36.9	15.935	0.015	3.072	2.669	18.6813	290.5198	305	3.34
2460911.53092	15.508	0.013	15.451	0.015	15.415	0.018	37.8	15.455	0.015	2.759	2.606	21.4902	294.1352	161	2.60
2460913.52832	15.450	0.027	15.382	0.031	15.351	0.037	37.9	15.386	0.030	2.697	2.597	21.9124	294.9587	30	0.46
2460927.48611	14.561	0.016	14.453	0.015	14.374	0.016	38.5	14.452	0.015	2.280	2.555	23.1730	301.9335	40	0.55
2460928.48232	14.479	0.015	14.371	0.014	14.294	0.015	38.6	14.370	0.014	2.251	2.553	23.1333	302.5287	44	0.51
2460929.48056	14.411	0.022	14.286	0.019	14.180	0.023	38.6	14.284	0.018	2.223	2.550	23.0739	303.1406	39	0.45
2460930.49017	14.273	0.043	14.120	0.034	13.990	0.030	38.6	14.116	0.033	2.194	2.548	22.9935	303.7754	4	0.05
2460932.47974	14.246	0.071	14.076	0.076	13.935	0.082	38.7	14.071	0.073	2.139	2.544	22.7737	305.0758	16	0.10

Notes.
[a] Using 28.″6 aperture.
[b] Using 38.″4 aperture.
[c] Using 46.″3 aperture.
[d] Size in arcseconds of the 7×10^4 km linear aperture.
[e] Heliocentric distance of 3I/ATLAS.
[f] Geocentric distance of 3I/ATLAS.
[g] Sun–3I/ATLAS–Earth angle.
[h] Apparent true anomaly of 3I/ATLAS in its heliocentric orbit.
[i] Number of individual photometric measurements contributing to the binned value.
[j] The timespan of the individual observations that are binned together.

The bluer wavelength range of HATPI may be picking up gas emission in addition to scattering of optical light by dust in the coma. Preperihelion spectroscopic observations by W. B. Hoogendam et al. (2025b), covering the time period up to 2025 September 2, show Ni, Fe, and CN emission lines. The reddest of these are the CN lines around 387 nm, which are outside the blue cutoff of the HATPI bandpass. Similarly, L. E. Salazar Manzano et al. (2025) detect the CN lines, in observations made in 2025 August, but do not detect redder emission that might come from C_3 or C_2 lines. Postperihelion observations by W. B. Hoogendam et al. (2026) do show C_2 emission lines that are within the HATPI bandpass. It is unclear, however, whether such AN emission could have been present during the latest HATPI observations obtained before perihelion, between 2025 September 8 and 13.

Because HATPI has a lower spatial resolution than ATLAS, NOT, ZTF, or SNIFS, we are forced to use a larger photometric aperture that picks up more of the extended tail of the comet. Differences between the extended tail of the comet and the inner coma (e.g., in the dust composition, scattering properties, gas emission, or in the phase dependence) could also be responsible for the steeper heliocentric index seen in the HATPI observations. A hint of this can be seen by adopting a larger linear aperture of 8×10^4 km, such that the largest angular-size aperture is used when 3I/ATLAS achieves the smallest value of Δ within the HATPI observations. Using the 8×10^4 km aperture leads to a slightly steeper heliocentric index of $n = 5.31 \pm 0.11$ compared to $n = 5.167 \pm 0.095$ when using the 7×10^4 km aperture.

We also note that a steeper heliocentric index is expected for H_2O sublimation and spectroscopic observations by SPHEREx in early August have revealed significant water gas emission in addition to CO_2 emission (C. M. Lisse et al. 2025a). H_2O has also been seen in postperihelion observations by C. M. Lisse et al. (2026).

We also note that comets typically change color as they approach perihelion, becoming bluer over time. J. Tonry et al. (2025) noted a change in color for 3I/ATLAS, which they observed to become bluer after 2025 July 13. This could also manifest as a steeper power-law index in a bluer filter, though the synthetic SNIFS *g*-band photometry from W. B. Hoogendam et al. (2025b) appears to be well-fitted by the same power-law used to fit all of the observations. Our assumption of a fixed Gaia color when converting the HATPI measurements to Gaia *G*-band is also inaccurate in this sense and could lead to a $\sim$0.02 mag systematic error over the course of the observations. Such a shift is too small to be responsible for the steeper rise in brightness seen in the HATPI observations.

4. Conclusion

In this paper, we have reported time-series photometry observations of the interstellar comet 3I/ATLAS obtained with the HATPI instrument. This is the first report of moving object time-series photometry from the HATPI facility and we describe the methods we have used to extract these measurements, together with our process for identifying clean photometry measurements.

A total of 7294 clean 45 s photometric measurements of 3I/ATLAS were obtained over 46 nights between 2025 May 2 and 2025 September 13, inclusive. After binning all observations obtained on a given night, we find that HATPI first robustly recovers 3I/ATLAS on the night of 2025 July 2, at a Gaia *G*-band magnitude of 17.796 ± 0.082 mag. The earliest night on which 3I/ATLAS is detected in individual 45 s exposures is 2025 August 6. We do not see any clear intra-night variability at short timescales above $\sim$0.2 mag after this date.

The nightly binned HATPI observations are well-fitted as a power-law function of the heliocentric distance, with a heliocentric index of $n = 5.167 \pm 0.095$. This is steeper than the dependence seen in other light curves in the literature. A simultaneous fit to the observations from HATPI, NOT, ATLAS, ZTF, TESS, and SNIFS yields a heliocentric index of $n = 3.94 \pm 0.10$, and a phase function of $\beta = 0.0552 \pm 0.0032$ mag day^{-1}. The steeper dependence of HATPI may be due to the larger photometric aperture for HATPI that picks up more of the extended tail of the comet. It is also possible that the HATPI bandpass includes gas emission lines, though emission lines within the HATPI bandpass were not detected in preperihilion spectra of 3I/ATLAS.

Thanks to its massive field of view, and continuous high-cadence monitoring, numerous moving objects have been observed by HATPI already and will be observed in the future. The processes that we have outlined in this paper can be applied to these objects as well, including many objects that have not received the same degree of intensive targeted observation as 3I/ATLAS.

Acknowledgments

We thank the anonymous referee for their helpful comments, which have improved the quality of this work. Funding for developing and prototyping the HATPI system and initial construction was provided by the David and Lucile Packard Foundation. Funding for the construction and operation of HATPI has been provided by the Gordon and Betty Moore Foundation. The Mt. Cuba Astronomical Foundation funded the construction of the HATPI mount. Data presented here is based on observations obtained with HATPI, stationed at the Las Campanas Observatory of Carnegie Science. We thank the Observatory, staff, and management, for hosting HATPI at this world-class facility and providing support for its operations. We thank the Jet Propulsion Laboratory (JPL) for providing access to the HORIZONS ephemeris computation service for generating solar system object trajectories. A.J. acknowledges support from Fondecyt project 1251439. G.J.T. acknowledges support from the UK Space Agency as part of its support for the UK component of the PLATO Mission.

Facilities: Gaia, NOT, TESS, ATLAS.

Software: FITSH (A. Pál 2012), Astropy (Astropy Collaboration et al. 2013, 2018, 2022), VARTOOLS (J. D. Hartman & G. Á. Bakos 2016).

ORCID iDs

Joel D. Hartman https://orcid.org/0000-0001-8732-6166
Gáspár Á. Bakos https://orcid.org/0000-0001-7204-6727
Andrés Jordán https://orcid.org/0000-0002-5389-3944
Sarah Thiele https://orcid.org/0000-0001-7442-6926
Zoltán Csubry https://orcid.org/0000-0002-8423-0510
Geert Jan Talens https://orcid.org/0000-0003-4787-2335
Attila Bódi https://orcid.org/0000-0002-8585-4544
Anthony Keyes https://orcid.org/0009-0007-3707-4846

Adriana Gaitan https://orcid.org/0009-0000-7483-4495
Antoine Thibault https://orcid.org/0009-0004-3477-9064

References

Ahuja, G., & Ganesh, S. 2025, ApJL, 995, L13
Ahuja, G., & Ganesh, S. 2026, RNAAS, 10, 19
Alard, C., & Lupton, R. H. 1998, ApJ, 503, 325
Alvarez-Candal, A., Rizos, J. L., Lara, L. M., et al. 2025, A&A, 700, L10
Andrae, R., Fouesneau, M., Creevey, O., et al. 2018, A&A, 616, A8
Astropy Collaboration, Price-Whelan, A. M., Lim, P. L., et al. 2022, ApJ, 935, 167
Astropy Collaboration, Price-Whelan, A. M., Sipőcz, B. M., et al. 2018, AJ, 156, 123
Astropy Collaboration, Robitaille, T. P., Tollerud, E. J., et al. 2013, A&A, 558, A33
Barbieri, M., & Loeb, A. 2026, RNAAS, 10, 17
Belyakov, M., Fremling, C., Graham, M. J., et al. 2025, RNAAS, 9, 194
Belyakov, M., Wong, I., Bolin, B. T., et al. 2026, arXiv:2601.22034
Beniyama, J. 2025, PASJ, 77, L71
Bolin, B. T., Belyakov, M., Fremling, C., et al. 2025, MNRAS, 542, L139
Borisov, G., Birtwhistle, P., Bacci, P., et al. 2019, CBET, 4666, 1
Borlaff, A. S., Marcum, P. M., & Howell, S. B. 2025, Natur, 648, 51
Chandler, C. O., Bernardinelli, P. H., Jurić, M., et al. 2025, arXiv:2507.13409
Choi, S., Ishiguro, M., Takahashi, J., et al. 2026, ApJL, 1000, L29
Cloete, R., Loeb, A., & Vereš, P. 2025, arXiv:2509.21408
Combi, M. R., Mâkinen, T., Bertaux, J.-L., et al. 2025, arXiv:2512.22354
Cordiner, M. A., Roth, N. X., Kelley, M. S. P., et al. 2025, ApJL, 991, L43
Coulson, I. M., Kuan, Y.-J., Charnley, S. B., et al. 2026, MNRAS, 546, stag063
de la Fuente Marcos, R., Alarcon, M. R., Licandro, J., et al. 2025, A&A, 700, L9
Denneau, L., Siverd, R., Tonry, J., et al. 2025, MPES, 2025-N12
Eubanks, T. M., DeForest, C. E., Walsh, K. J., et al. 2025, RNAAS, 9, 324
Feinstein, A. D., Noonan, J. W., & Seligman, D. Z. 2025, ApJL, 991, L2
Forbes, J. C., & Butler, H. 2026, RNAAS, 10, 12
Frincke, T. T., Yaginuma, A., Noonan, J. W., et al. 2025, MNRAS,
Gaia Collaboration, Brown, A. G. A., Vallenari, A., et al. 2018, A&A, 616, A1
Gray, Z., Bagnulo, S., Borisov, G., et al. 2025, ApJL, 992, L29
Guo, Y., Zhang, L., Feng, F., et al. 2025, AJ, 170, 362
Hartman, J. D., & Bakos, G. Á. 2016, A&C, 17, 1
Hibberd, A., Crowl, A., & Loeb, A. 2025, arXiv:2507.12213
Hibberd, A., Eubanks, T. M., & Hein, A. 2026, arXiv:2601.02533
Hinkle, J. T., Yang, B., Meech, K. J., et al. 2025, arXiv:2512.02106
Hoogendam, W. B., Jones, D. O., Yang, B., et al. 2026, arXiv:2601.16983
Hoogendam, W. B., Kuesters, D., Shappee, B. J., et al. 2025b, arXiv:2512.09020
Hoogendam, W. B., Shappee, B. J., Wray, J. J., et al. 2025a, arXiv:2510.11779
Hopkins, M. J., Dorsey, R. C., Forbes, J. C., et al. 2025, ApJL, 990, L30
Hui, M.-T., Jewitt, D., Mutchler, M. J., Agarwal, J., & Kim, Y. 2026, ApJL, 999, L37
Hutsemékers, D., Manfroid, J., Jehin, E., et al. 2026, A&A, 706, A43
Jacobson-Bell, B., Croft, S., White, E., et al. 2025, RNAAS, 9, 351
Jayasinghe, T., Stanek, K. Z., Kochanek, C. S., et al. 2019, MNRAS, 486, 1907
Jewitt, D., Hui, M.-T., Mutchler, M., Kim, Y., & Agarwal, J. 2025, ApJL, 990, L2
Jewitt, D., & Luu, J. 2025, ApJL, 994, L3
Kareta, T., Champagne, C., McClure, L., et al. 2025, ApJL, 990, L65
Keto, E., & Loeb, A. 2026, MNRAS, 545, staf2054
Keto, E., & Loeb, A. 2025, arXiv:2510.18157
Lang, D., Hogg, D. W., Mierle, K., Blanton, M., & Roweis, S. 2010, AJ, 139, 1782
Lisse, C. M., Bach, Y. P., Bryan, S. A., et al. 2025a, arXiv:2512.07318
Lisse, C. M., Bach, Y. P., Bryan, S., et al. 2025b, RNAAS, 9, 242
Lisse, C. M., Bach, Y. P., Bryan, S. A., et al. 2026, RNAAS, 10, 26
Maggiolo, R., Dhooghe, F., Gronoff, G. P., de Keyser, J., & Cessateur, G. 2026, ApJL, 996, L34
Martinez-Palomera, J., Tuson, A., Hedges, C., et al. 2025, ApJL, 994, L51
Meech, K. J., Weryk, R., Micheli, M., et al. 2017, Natur, 552, 378
Neukart, F. 2025, arXiv:2511.07450
Opitom, C., Snodgrass, C., Jehin, E., et al. 2025, MNRAS, 544, L31
Pál, A. 2012, MNRAS, 421, 1825
Pérez-Couto, X., Torres, S., Villaver, E., Mustill, A. J., & Manteiga, M. 2025, arXiv:2509.07678
Puzia, T. H., Rahatgaonkar, R., Carvajal, J. P., Nayak, P. K., & Luco, B. 2025, ApJL, 990, L27
Rahatgaonkar, R., Carvajal, J. P., Puzia, T. H., et al. 2025, ApJL, 995, L34
Roth, N. X., Cordiner, M. A., Bockelée-Morvan, D., et al. 2026, ApJL, 999, L32
Salazar Manzano, L. E., Lin, H. W., Taylor, A. G., et al. 2025, ApJL, 993, L23
Santana-Ros, T., Ivanova, O., Mykhailova, S., et al. 2025, A&A, 702, L3
Scarmato, T. 2025a, arXiv:2511.19467
Scarmato, T. 2025b, arXiv:2512.22365
Scarmato, T., & Loeb, A. 2026, arXiv:2601.10860
Seligman, D. Z., Micheli, M., Farnocchia, D., et al. 2025, ApJL, 989, L36
Serra-Ricart, M., Licandro, J., & Alarcon, M. R. 2026, A&A, 705, L3
Sheikh, S. Z., Garcia Lopez, V., Gerrard, I., et al. 2025, arXiv:2512.18142
Steffen, M. 1990, A&A, 239, 443
Tan, H., Yan, X., & Li, J.-Y. 2026, arXiv:2601.15443
Taylor, A. G., & Seligman, D. Z. 2025, ApJL, 990, L14
Tonry, J., Denneau, L., Alarcon, M., et al. 2025, ApJL, 995, L15
Trigo-Rodríguez, J. M., Gritsevich, M., & Blum, J. 2025, arXiv:2511.19112
Xing, Z., Oset, S., Noonan, J., & Bodewits, D. 2025, ApJL, 991, L50
Yaginuma, A., Taylor, A. G., & Seligman, D. Z. 2026, MNRAS,
Yang, B., Meech, K. J., Connelley, M., Zhao, R., & Keane, J. V. 2025, ApJL, 992, L9
Ye, Q., Kelley, M. S. P., Hsieh, H. H., et al. 2025, ApJL, 993, L31
Zechmeister, M., & Kürster, M. 2009, A&A, 496, 577
Zhang, Q., & Battams, K. 2026, PASP, 138, 014403